Mon. Not. R. Astron. Soc. **000**, 1–?? (0000) Printed 12 January 2016 (MN LATEX style file v2.2)

Deciphering the bipolar planetary nebula Abell 14 with 3D ionization and morphological studies

S. Akras[1⋆], N. Clyne[1,2], P. Boumis[3], H. Monteiro[4], D. R. Gonçalves[1], M. P. Redman[2], S. Williams[3]

[1] *Observatório do Valongo, Universidade Federal do Rio de Janeiro, Ladeira Pedro Antonio 43 20080-090 Rio de Janeiro, Brazil*
[2] *Centre for Astronomy, School of Physics, National University of Ireland Galway, University Road, Galway, Ireland*
[3] *Institute for Astronomy, Astrophysics, Space Applications and Remote Sensing, National Observatory of Athens, I. Metaxa & V. Pavlou, Penteli, GR–15236, Athens, Greece*
[4] *Instituto de Física e Química, Universidade Federal de Itajubá, Brasil*

arXiv:1601.02170v1 [astro-ph.SR] 10 Jan 2016

Received **insert**; Accepted **insert****

ABSTRACT

Abell 14 is a poorly studied object despite being considered a born again planetary nebula. We performed a detailed study of its 3D morphology and ionization structure using the SHAPE and MOCASSIN codes. We found that Abell 14 is a highly evolved, bipolar nebula with a kinematical age of ∼19,400 yr for a distance of 4 kpc. The high He abundance, and N/O ratio indicate a progenitor of 5 $M_{\odot}$ that has experienced the third dredge–up and hot bottom burning phases. The stellar parameters of the central source reveal a star at a highly evolved stage near to the white dwarf cooling track, being inconsistent with the born again scenario. The nebula shows unexpectedly strong [N I] λ5200 and [O I] λ6300 emission lines indicating possible shock interactions. Abell 14 appears to be a member of a small group of highly evolved, extreme Type–I PNe. The members of this group lie at the lower-left corner of the PNe regime on the [N II]/Hα vs. [S II]/Hα diagnostic diagram, where shock–excited regions/objects are also placed. The low luminosity of their central stars, in conjunction with the large physical size of the nebulae, result in a very low photo–ionization rate, which can make any contribution of shock interaction easily perceptible, even for small velocities.

Key words: ISM: kinematics and dynamics — ISM: abundances — binaries: general — planetary nebulae: individual: Abell 14

1 INTRODUCTION

Planetary nebulae (PNe) represent the final product of the interaction between a slow and dense stellar wind that originates from an Asymptotic Giant Branch (AGB) star, and a subsequent, faster and tenuous wind expelled between the very late AGB phase and at the beginning of the post–AGB phase. The interaction between these two stellar winds results in the formation of a PN (Interacting stellar wind model; Kwok et al. 1978). This model can adequately explain the formation of spherically symmetric PNe.

Nevertheless, the majority of PNe and proto–PNe show asymmetric and complex morphologies (Boumis et al. 2003, 2006; Parker et al. 2006; Manchado et al. 2011; Sahai et al. 2011; Sabin et al. 2014) that can not be explained by the ISW model. As a consequence, the development of a more general picture, which employs an axisymmetric equatorial density enhancement in the AGB wind (generalized ISW; see Balick & Frank 2002), has been established as the standard model to explain the formation of non–spherically symmetric PNe.

The formation mechanism for the equatorial density enhancement in the AGB wind is, however, still poorly understood. The most likely mechanisms are (i) the presence of magnetic fields (Chevalier & Luo 1994; García–Segura & López 2000; Frank & Blackman 2004; Vlemmings 2012) or (ii) the interaction of a close binary nucleus during the post–common envelope phase (Iben & Livio 1993; Soker & Livio 1994; Soker & Rappaport 2001; Jones et al. 2012). The magnetic fields alone may not be unable to provide sufficient angular momentum needed to form aspherical PNe (Soker 2006, Nordhaus & Blackman 2007, García–Segura et al. 2014). On other hand, only a small number of PNe have been found to host a close binary nucleus (∼50; see Jones et al. 2015 and references therein), which conflicts with the number of known aspherical PNe (de Marco 2009, Miszalski et al. 2011a,b). Moreover, the number of ∼50 PNe with close binary nucleus corresponds to a small percentage of the total

⋆ e-mail:akras@astro.ufrj.br

© 0000 RAS

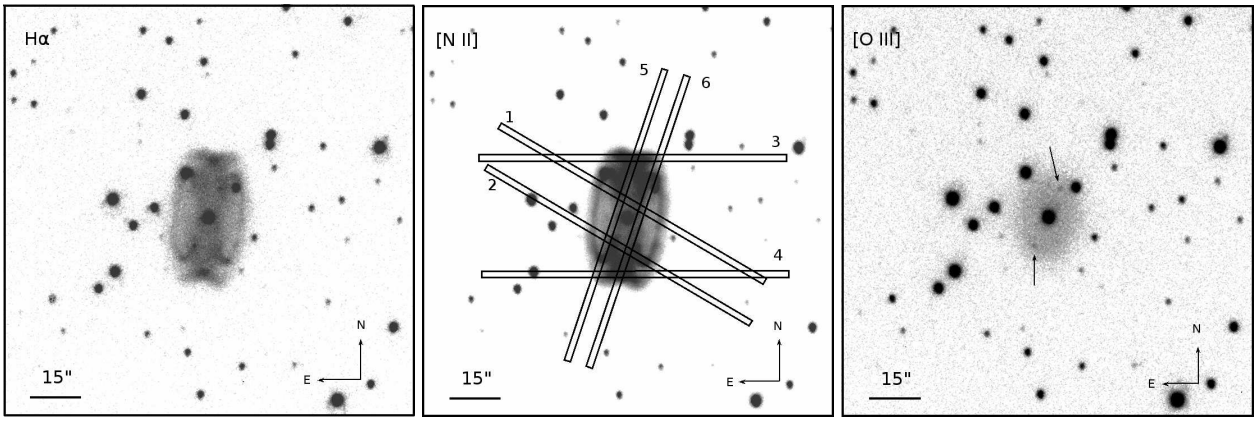

Figure 1. Hα, [N II], and [O III] images of Abell 14 obtained with the 2.3 m Aristarchos telescope. The field size for the images shown is 120×120 arcsec. The MES–SPM slit positions are overlaid on the [N II] image. The width of each rectangle corresponds to a slit width of 1.9 arcsec and the slit length is equal to 90 arcsec. The two arrows on the [O III] image indicates the presence of two field stars.

number of known PNe in our Galaxy (∼3500; e.g. Kwitter et al. 2014; Sabin et al. 2014. In order to address this question, bipolar planetary nebulae that exhibit extreme or unusual properties can be investigated, and if these sources can be understood they will help in resolving the question of the shaping mechanism for PNe.

The motivation for this work comes from the noticeable differences between the optical spectra (emission line intensities) and the chemical abundances of the PN Abell 14 or PN A66 14 (Abell 1966) derived by Bohigas 2003 (hereafter B03) and Henry et al. 2010 (hereafter H10), as well as its classification as a possible born–again nebula by de Marco (2009). We performed a morpho–kinematical study of Abell 14 by means of high–dispersion, long–slit spectra and the the astronomical code SHAPE[1] (Steffen & López 2006, Steffen et al. 2011) in order to construct the 3D structure of the nebula. The 3D density distribution from our best–fit SHAPE model was used as an input to the 3D photo–ionization code MOCASSIN (Ercolano et al. 2003, 2005, 2008) in order to perform a more detailed study of its ionization structure and derive the fundamental physical parameters of the central source and the nebula.

The manuscript is organized as follows: In Section 2, we present a detailed description of Abell 14. The observations and data reduction procedures are presented in Section 3. In Section 4, we present the results from the 3D analysis of Abell 14, and describe our 3D modelling with the codes SHAPE and MOCASSIN. Our morpho–kinematic and physico–chemical results are discussed in Section 5. Conclusions are summarized in Section 6.

2 ABELL 14

The central star of Abell 14 has been classified as a massive blue giant B5 III–V ($V = 15.24$ and $B-V = 0.51$) by Lutz & Kaler (1987) and more recently as a B8–9 star by Weidmann & Gamen (2011). Interestingly, these observational results do not agree with the stellar properties derived by studying the properties of its surrounding nebula (B03). In particular, the author has found that the central star of Abell 14 should be a hot star with a Zanstra temperature of 150,000 K and a low visual magnitude of $V_o = 22.9 \pm 0.3$, using the formula given in Jacoby & Kaler (1989) for optically thick PNe, despite Abell 14 is an optically thin PN. This suggests that the central star of Abell 14 may be a binary system containing a hot, faint companion and a type B giant star. According to the evolutionary models from Vassiliadis & Wood (1994) and Blöcker (1995), B03 estimated the initial mass of the progenitor star to be between 2.5 and 3 $M_{\odot}$, with an evolutionary age of ∼8,000 yr.

B03 and H10 studied the chemical properties of Abell 14, and there are notable differences between the two studies. In particular, the intensities of the [O III] $\lambda\lambda 4959, 5007$ emission lines from H10 are ∼1.6 times larger than those from B03. The [O I] $\lambda 6300$ line is detected by H10 with [O I]/H$\beta = 30$, while it is not found by B03 despite the detection of the fainter He I $\lambda 5876$ line (He I/H$\beta = 15.6$). The [N I] $\lambda 5200$ line, which could be associated with strong shock interactions, is detected by B03 but not by H10. The logarithmic dereddened Hβ fluxes are also slightly different between the two studies: logF(Hβ) = −14.23 (B03) and −14.82 (H10). These differences may be related to the slit positions where the spectra were obtained: along the north–south direction (PA=0°; B03), and along the east–west direction (PA=100°; H10). More recently, Frew et al. (2013) published a total integrated Hα flux of −12.45, which is close to the value of −12.27 quoted by B03.

Regarding the chemical abundances, H10 calculated higher He, N, and O than those derived in B03 by factors of 1.25, 2.7, and 1.95, respectively, and lower S and Ar abundances by factors of 0.34 and 0.68, respectively. However, both studies agree that Abell 14 is an extremely nitrogen–rich nebula with log(N/O) = 0.48 (B03) and 0.62 (H10). A similarly high N/O abundance ratio has been found in highly evolved bipolar PNe such as PN G321.6+02.2 (Corradi et al. 1997), HaTr 10 (Tajitsu et al. 1999), RCW 24 and RCW 69 (Frew et al. 2006), and PN G342.0-01.7 (Ali et al. 2015). Each of these PNe exhibits very low electron density (N_e) and very hot, optically faint central star, like that of Abell 14. The connection of these PNe with Abell 14 is discussed in § 6.

[1] http://www.astrosen.unam.mx/shape/

Table 1. Observation log

Slit	Filter	Date	PA/Offset (°)/(″)	Exp. (s)
		2.1 m SPM Spectroscopy	Observatory	
1	Hα+[N II]	21–11–2012	59 / 4 N	1800
2	Hα+[N II]	21–11–2012	59 / 12 S	1800
3	Hα+[N II]	21–11–2012	87 / 17 N	1800
4	Hα+[N II]	21–11–2012	87 / 17 S	1800
5	Hα+[N II]	22–11–2012	341 / 5 E	1800
6	Hα+[N II]	22–11–2012	341 / 5 W	1800
6	[O III]	26–03–2015	341 / 5 W	1800
		2.3 m Helmos Imaging	Observatory	
-	Hα	08–11–2013	–	1800
-	[N II]	08–11–2013	–	1800
-	[O III]	08–11–2013	–	1800

Unlike the chemical abundances and line intensities, the N_e[S II], T_e[N II], and $c(H\beta)$ parameters are in agreement within the errors between the two aforementioned studies. The more recent value of $c(H\beta) = 1.52$, reported by Giammanco et al. (2011), is significantly higher than the previous reported values from B03 (0.98) and H10 (0.88). The extremely low N_e values of 55 cm^{-3} (H10) and 85 cm^{-3} (B03) indicate an old nebula. It should be mentioned that these values suffer from high levels of uncertainty. In particular, the errors of N_e have been estimated to be 165 cm^{-3} (H10) and $^{+70}_{-60}$ cm^{-3} (B03), respectively. According to this, an N_e value of $\leqslant$200 cm^{-3} should be considered as more reasonable for this nebula.

Regarding the distance of Abell 14, it still remains poorly constrained in the literature with reported values of 3.32 kpc (Cahn et al. 1992), 3.38 kpc (Stanghellini & Haywood 2010), 5.40 kpc (Giammanco et al. 2011), 7.25 kpc (Zhang 1995), and 2.66 to 3.77 kpc (Phillips 2004). The bipolar structure of this nebula introduces a high level of uncertainty to its distance estimation and none of the aforementioned methods can be considered more reliable for this specific case. An average distance of 4.3 kpc with a standard deviation of 1.7 kpc is obtained from these measurements. This distance is found to be close to the value derived in this work based on 3D photo-ionization models (see §4.3).

3 OBSERVATIONS

3.1 Optical imaging

New high–quality optical images of Abell 14 were obtained with the 2.3 m Ritchey–Chretien Aristarchos telescope (f/8) at the Helmos Observatory in Greece on 2013 November 8. The observations were taken with a 1024×1024 SITe CCD detector consisting of 24 μm^2 pixels. The field of view and image scale were 5×5 arcmin^2 and 0.28 arcsec pixel^{-1}, respectively. Exposures of 1800 s were obtained through 17, 17, and 30 Å bandwidth filters centred on the Hα (λ6567), [N II] (λ6588), and [O III] (λ5011) nebular emission lines (Table 1). During observations, the seeing varied between 1.1 and 1.3 arcsec. Individual images were bias subtracted, flat–field corrected, and cleaned of cosmic rays using standard routines in IRAF[2]. The processed images are shown in Fig. 1.

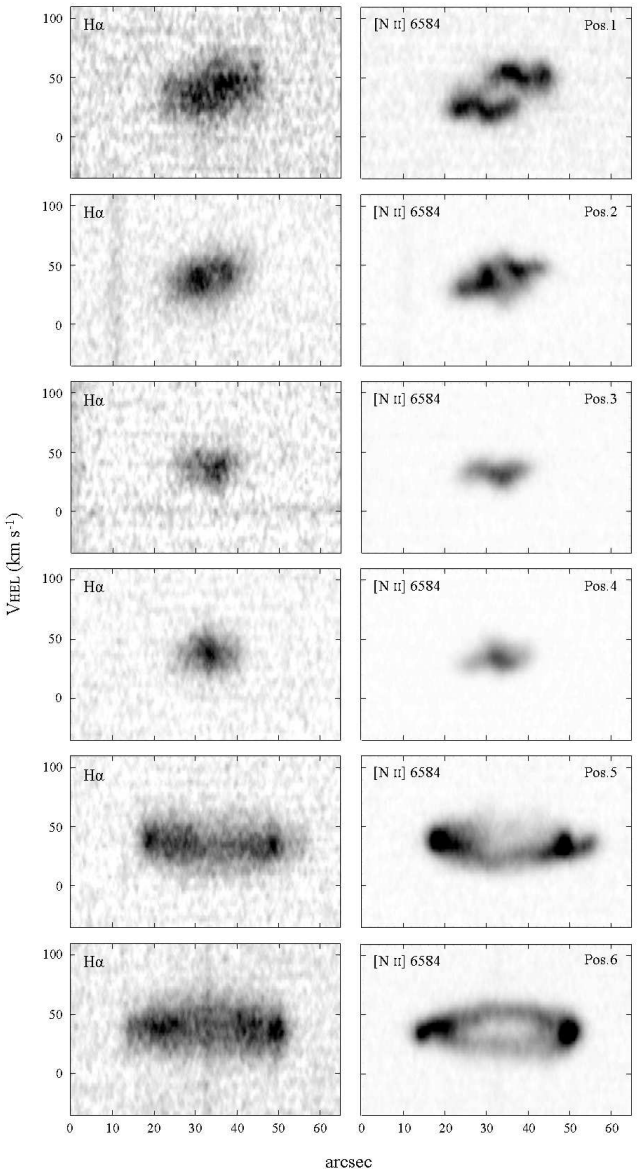

Figure 2. Hα (left–hand column) and [N II] λ6584 (right–hand column) PV diagrams of Abell 14 for 6 slit positions.

3.2 High-resolution spectroscopy

High–resolution, long–slit spectroscopic data of Abell 14 were obtained in Hα+[N II] and [O III] using the Manchester Echelle Spectrometer (MES–SPM; Meaburn et al. 2003) on the 2.1 m telescope at the San Pedro Martir Observatory in

[2] IRAF (Image Reduction and Analysis Facility) is distributed by the National Optical Astronomy Observatory, which is operated by he Association of Universities for Research in Astronomy (AURA) Inc., under cooperative agreement with the National Science Foundation.

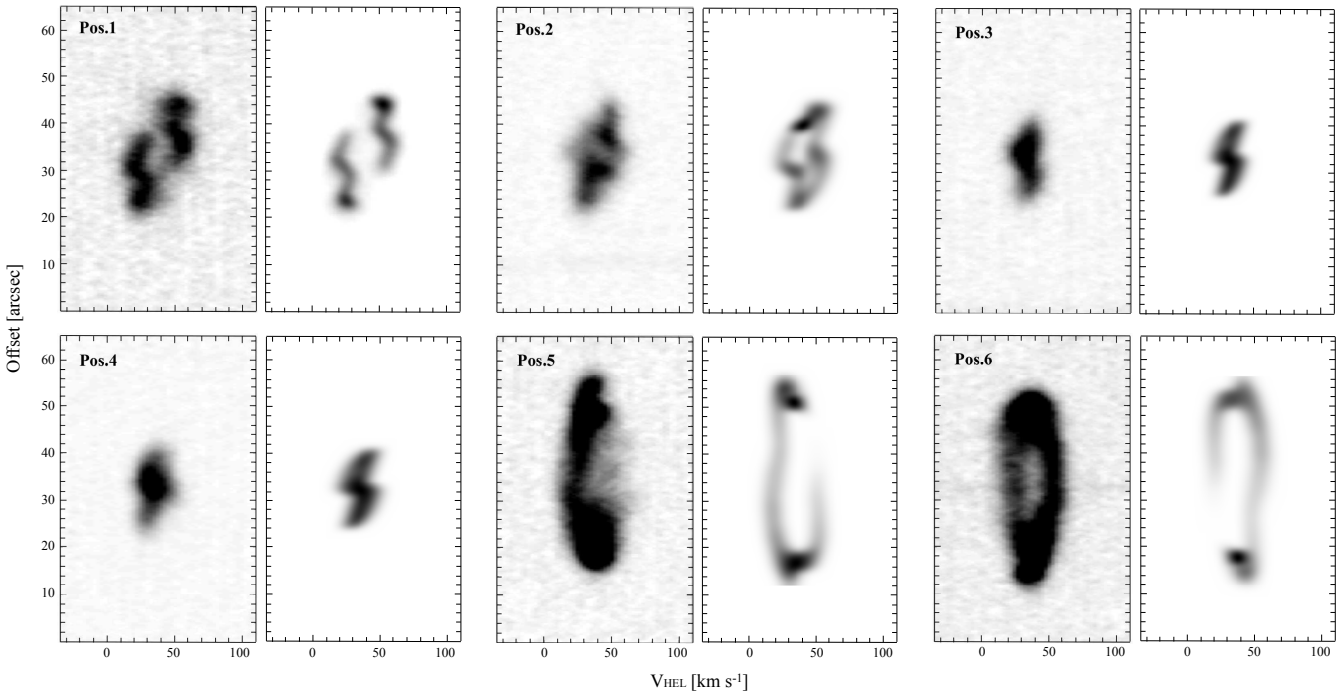

Figure 3. Observed [N II] λ6584 and synthetic PV diagrams of Abell 14 for 6 slit positions. The systemic velocity $V_{\rm sys} = 40$ km s^{-1}.

Baja California, Mexico, in its f/7.5 configuration. The observing runs took place on 2012, 21-22 November and 2015, 26 March (Table 1).

The MES–SPM was equipped with a Marconi 2048×2048 CCD with each square pixel 13.5 μm ($\equiv$0.176 arcsec pixel^{-1}) on each side. Bandwidth filters of 90 and 60 Å were used to isolate the 87$^{\rm th}$ and 113$^{\rm th}$ orders containing the Hα+[N II] $\lambda\lambda$6548, 6584 and [O III] λ5007 nebular emission lines. The [O III] λ5007 echelle spectrum is not presented here since it displays a simple ellispoidal structure with a very low expansion velocity. A binning of 2×2 was employed in both the spatial and spectral directions. Consequently, 1024 increments, each one 0.352 arcsec long, gave a projected slit length of ∼6 arcmin on the sky. The slit used was 150 μm wide ($\equiv$11.5 km s^{-1} or 1.9 arcsec). During the observations, the slits were oriented at different PAs (see Table 1) with an integration time of 1800 s for each orientation. All slit positions are shown overlaid on the [N II] image of Fig. 1.

The wavelength calibration was performed using a Th/Ar calibration lamp to an accuracy of $\pm$1 km s^{-1} when converted to a radial velocity. The data reduction was performed using the standard IRAF and STARLINK[3] packages. Individual images were bias subtracted and cosmic rays removed. The bi–dimensional line profiles or position-velocity (PV) diagrams are presented in Fig. 2.

[3] http://starlink.eao.hawaii.edu/starlink

4 ANALYSIS AND RESULTS

4.1 Morpho–kinematic analysis

Abell 14 displays an axially symmetric morphology in the Hα and [N II] emission lines with a size of 41×23 arcsec (Fig. 1). Two ring–like structures, each with a radius of 11.5 arcsec, are apparent to the east and west regions of the nebula, expanding with a de–projected velocity $V = 17 \pm 4$ km s^{-1}. Their bright [N II] emission seen in Fig. 1 is likely associated with shock interaction. In the [O III] image, the nebula shows more diffuse emission concentrated mostly in the central region with a size of 26×15 arcsec. This is consistent with the simple appearance of the [O III] line in the PV diagram discussed above. Two spots on opposite directions of the central star, indicated by arrows on the [O III] image of Fig. 1, are barely visible, and by scrutinizing the digital sky survey (DSS) images, we concluded that these two spots most likely correspond to very faint field stars.

The seemingly faint ring–like structure at the centre of the nebula, seen in Hα and [N II] lines, is the result of the projection effect, similar to those observed in two other PNe, namely SuWt 2 (Exter et al. 2010, Jones et al. 2010) and WeBo 1 (Tyndall et al. 2013). The nebular inclination and position angles with respect to the plane of the sky are found to be ∼24 and ∼5°, respectively.

Fig. 2 displays the observed PV diagrams for the Hα λ6563 and [N II] λ6584 emission lines for the slit positions 1 to 6. The PV diagrams in Hα reveal a more diffuse emission filling the internal volume of the nebula, whereas the [N II] emission originates from the outer parts of the nebula, like the walls of the bipolar lobes. The eastern and western parts of the nebula are blue– and red–shifted respectively, both with a de–projected velocity of $V_{\rm exp} = 25 \pm 4$ km s^{-1}. The

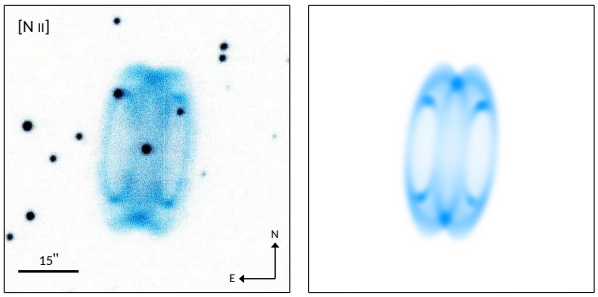

Figure 4. [N II] λ6584 image (left-hand) obtained from the Aristarchos telescope and the 2D rendered SHAPE image (right-hand). The F.O.V. of each image is 75 × 75 arcsec.

heliocentric systemic velocity of the nebula is estimated to be $V_{\rm sys} = 40 \pm 4$ km s^{-1}.

4.2 Shape modelling

A detailed morpho–kinematic study of Abell 14 was performed using the astronomical code SHAPE. Modelling with SHAPE mainly involves three steps. First, defining the geometrical forms to use; SHAPE has a variety of objects such as sphere, torus, cone, cube, etc., whose basic forms can be modified by the user (e.g. squeeze, twist, bump, etc). Second, an emissivity distribution is assigned to each individual structure that makes up the nebula. A third, a velocity law is chosen as a function of position from the geometrical centre. SHAPE produces a 2D image and synthetic PV diagrams that are rendered from the 3D model and compared visually with the observed data. The parameters of the model are then interactively adjusted until a satisfactory solution is obtained (e.g. Akras and Steffen 2012; Akras and López 2012; Clyne et al 2014; Clyne et al. 2015).

Our model of Abell 14 was constructed using the image and kinematic data from the [N II] λ6584 line due to its lower thermal broadening compared to that of the Hα line (thermal width of the Hα and [N II] lines at 10,000 K are 21.4 km s^{-1} and 5.8 km s^{-1}, respectively). This choise results in higher quality PV diagrams. An ellipsoidal shell was used to model the main body of the nebula, and was modified to conform with the observed image and PV diagrams. The model also includes two symmetrical rings that are positioned east and west of the nebular centre. The density of each component (ellipsoidal shell and both rings) was carefully modified by visually comparing and matching the contrast between the observed and synthetic PV diagrams. A homologous expansion velocity law of $v(r) = k(r/r_0)$ km s^{-1} was used, where r is the distance from the geometrical centre and r_0 is the reference radius as measured from the [N II] image. A key characteristic of a cylindrically symmetric and homologously expanding nebula is how the PV diagrams can be altered in such a way that the outline of the image and the PV diagram match up. This matching determines the factor of proportionality k in the mapping between position and velocity. It must however be noted that it is not possible to constrain the extent of the nebula along the line of sight and thus more than one solution can be found to fit the data.

For our best–fit model, k=21 km s^{-1} arcsec^{-1} and

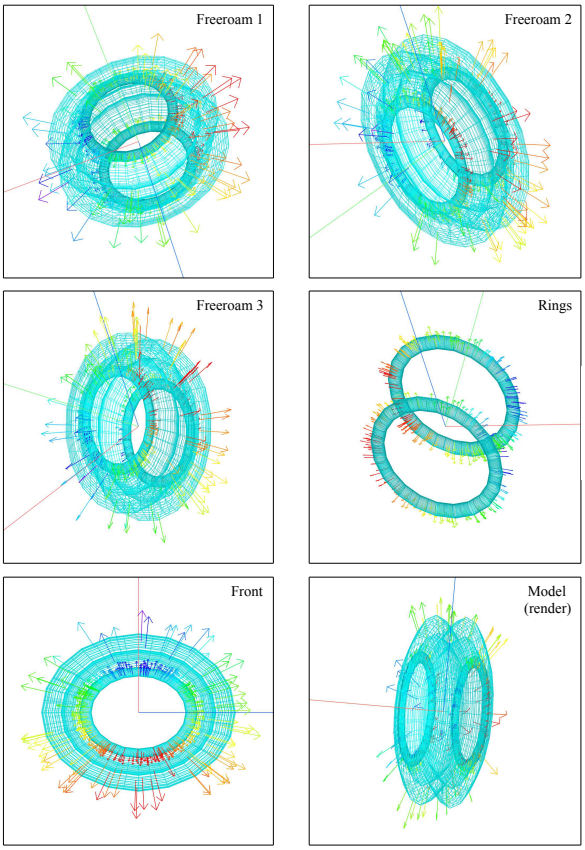

Figure 5. Mesh images of Abell 14 in three random orientations, labeled as Freeroam 1, 2 and 3, showing its nebular components and velocity fields. The blue and red vectors correspond to the blue– and red–shifted parts of each component.

r_0=21.5 arcsec were derived for the main nebular structure. For each slit position, the resultant synthetic PV diagrams are placed side by side with the observed PV diagrams, as shown in Fig. 3. The observed [N II] image and that from the best–fit model are illustrated in Fig. 4. The 3D mesh structure of the model with the Doppler–colour velocity fields at six different orientations are presented in Fig. 5 for a better visualization of the 3D structure of the nebula.

The modelled inclination angle along the east–west direction with respect to the plane of the sky is 22° ± 4°, whereas it is zero along the north–south direction. The de–projected expansion velocity of the outer [N II] shell in the equatorial direction is 21 km s^{-1}. This implies that for a distance D in kpc, and a constant expansion law, the kinematical age of the nebula is $tD^{-1} = 4,850 \pm 870$ yr kpc^{-1}. Using the lowest (3.32 kpc) and highest (7.25 kpc) literature distances of Abell 14 (see §2), its equatorial size is estimated between 0.34 and 0.75 pc, which are reasonable values for highly evolved PNe (hereafter HE–PNe), whereas its kinematical age is between 16,000 and 35,000 yr. Notice that these ages do not agree with the evolutionary age of ∼8,000 yr, proposed by B03, because of the assumption that its central star has a $L \sim 200\ L_\odot$ which is several times larger than the value found in this work (see §4.3).

For the ring–like structures, which have a radius of

Table 2. Observational fluxes and empirical abundance, as well as input parameters and line fluxes for the models studied in this work.

	B03[a]	H10[b]	MOD1[c]	MOD2[d]	MOD3[e]	MOD4[f]
Source						
H:He:CNO(%)	–	–	91:9:0.1	MOD1	MOD1	0:33:67
T⋆ (kK)	151	–	150	150	120	120
L⋆/L$_\odot$	–	–	200	15	15	15
log(g)	–	–	7	7	7	7
Abundance						
He/H	0.16	0.196	0.16	0.196	0.16	0.16
C/H (10^{-4})[g]	–	–	–	–	4.6	4.6
N/H (10^{-4})	3.90	10.5	3.90	10.5	6.0	8.0
O/H (10^{-4})	1.30	2.54	1.30	2.54	2.1	3.0
Ne/H (10^{-5})	–	9.79	–	9.79	9.8	9.8
S/H (10^{-6})	9.30	3.15	9.30	3.15	12.0	20.0
Ar/H (10^{-6})	2.10	1.46	2.10	1.46	1.5	1.5
Cl/H (10^{-8})	–	–	–	–	1.0	1.0
He I 5876	0.16	0.22	0.02	0.24	0.20	0.24
He II 4846	0.34	0.26	1.61	0.45	0.33	0.34
[N I] 5200	0.29	–	0.00	0.00	0.00	0.00
[N II] 5755	0.29	0.41	0.02	0.16	0.16	0.05
[N II] 6548	4.79	5.5	0.36	5.41	4.8	4.51
[N II] 6584	14.35	16	1.09	16.2	14.3	13.6
[O I] 6300	–	0.3	0.00	0.02	0.06	0.02
[O III] 4363	–	–	0.10	0.05	0.04	0.01
[O III] 4959	0.98	1.6	1.71	1.72	1.40	0.75
[O III] 5007	3.07	4.8	5.14	5.15	4.20	2.24
[S II] 6717	0.57	0.66	0.03	0.08	0.70	0.42
[S II] 6731	0.43	0.49	0.02	0.06	0.53	0.32
$-\log(H\beta)$	13.24	13.85	13.70	13.70	13.70	13.60
Diagnostics						
N$_e$:						
[S II]$\frac{6731}{6717}$	0.75	0.74	0.79	0.76	0.76	0.76
T$_e$:						
[N II]$\frac{6584}{5755}$	65.9	52	40.	134.	121.	355.
[O III]$\frac{5007}{4363}$	—	—	66.	130.	138.	260.

[a] Slit width 3 arcsec oriented at north–south direction (PA=0°).
[b] Slit width 2 arcsec oriented at PA=100°.
[c] Model using B03 abundances and slit configuration.
[d] Model using H10 abundances and slit configuration.
[e] Best–fit model using H10 slit configuration as constraints.
[f] Best–fit model using H10 slit configuration as constraints and PG 1159 central star.
[g] The solar carbon abundance (Asplund et al. 2009) is assumed for the models MOD3 and MOD4

11.5 arcsec and a de–projected velocity of 16 km s^{-1}, we get a kinematical age of $tD^{-1} = 3,400 \pm 620$ yr kpc^{-1} or between 11,300 and 24,700 yr for the low and high literature estimates of the distance to Abell 14. This implies that the ring–like structures were formed during a more recent ejection event.

4.3 Mocassin modelling

In order to study the ionization structure of a bipolar PN, or even one with more complex 3D morphologies such as Abell 14, the use of sophisticated 3D photo–ionization codes is required. Our photo-ionization model was created with MOCASSIN (version 2.02.70), which is described in full detail in Ercolano et al. (2003, 2005, 2008) and that uses the atomic data files from the CHIANTI database (v. 7, Landi et al. 2012). The procedure of modelling Abell 14 requires to generate a density distribution of the nebular plasma and define the luminosity and effective temperature, the abundances for the most relevant elements and the distance of the nebula. Numerous models were generated until a good fit to the predefined constraints was found.

It is, however, a time consuming and trick task to generate an accurate 3D density distribution of the nebular plasma, which is why the density grid from our 3D SHAPE model was used as an input to the MOCASSIN code. It is important to point out that our SHAPE model was obtained using only the [N II] line, since the [O III] line exhibits a simple ellipsoidal structure. In order to get a density grid for the entire nebula (inner and outer regions), an ellipsoidal structure with an uniform density was simply added to the SHAPE density grid. This additional component is consistent

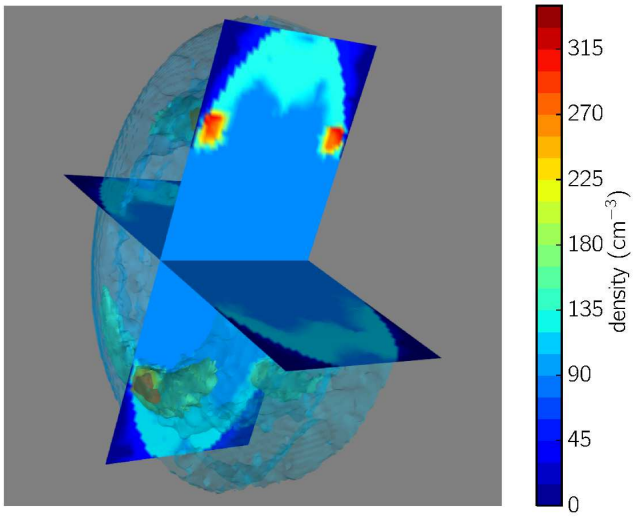

Figure 6. Cuts through the structure grid used as the input density distribution for the MOCASSIN model of Abell 14.

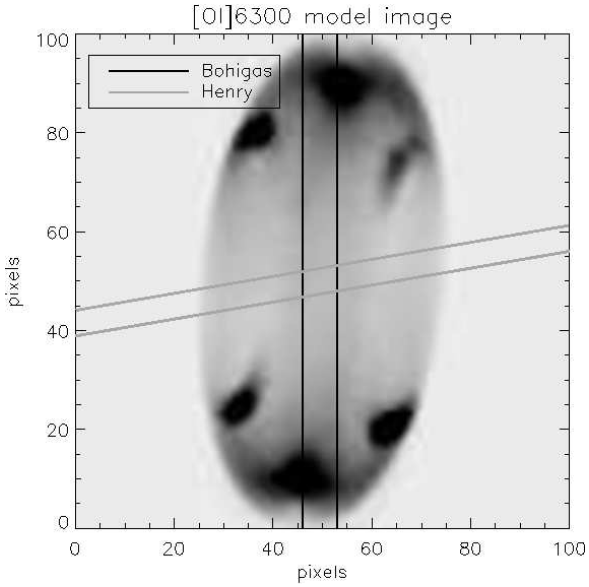

Figure 7. Projected [O I] λ6300 image obtained from the best–fit model with simulated slits overlaid. North is up and east is to the left.

with the observed [O III] 2D image and spectrum. The last necessary step before modelling was to adjust the SHAPE density grid, which comes in arbitrary units, in such a way that it successfully reproduces the [S II] $\lambda\lambda$6716, 6731 line ratio as well as constraints (Hβ flux, 2D-image, etc). The final structure used to produce the best modelled results is shown in Fig. 6.

Two sets of two long-slit spectra in different position angles obtained by B03 and H10 were used to constrain the model. The slit positions are shown in Fig. 7 overlaid on the best-fit model [O I] λ6300 image. As these data were not ideal for performing a 3D photo–ionization model – spatially resolved data (e.g. integral field unit; IFU) would be really advantageous for reproducing the spatial emission distribution of the nebula and study the ionization structure – it is important to keep this fact in mind when evaluating the model results presented in the next sections.

Besides the density distribution, another key element in photo–ionization modelling is the ionizing source. Recent developments in the modelling of stellar atmospheres have provided more complex stellar spectra that can be explored. Physical and chemical parameters such as log(g) and element abundances come into play. The standard choice of ionizing source models is the grid provided by T. Rauch, and described in detail in Rauch (2003), where the user can find NLTE stellar model atmosphere fluxes that cover the parameter range of PNe with hot central stars: $T_{\rm eff} = 50 - 190$ kK, log(g) $= 5 - 9$, and distinct abundances. In this work, we explored the ionizing sources of the second generation models including elements H−Ni, detailed Ca, as well as the iron-group (Sc+Ti+V+Cr+Mn+Fe+Co+Ni) opacities (MOD3). We also explored fits with atmosphere grid calculated from models with typical PG 1159 star abundance ratios; He:C:N:O = 33:50:2:15 by mass (MOD4).

Moreover, given that there are chemical abundances derived from the observed spectra (B03 and H10), we also ran models using the observed chemical abundances together with our density structure and ionizing source mentioned previously (see columns 2 and 3 in Table 2). We find that the modelled spectra (MOD1 and MOD2) are dissimilar from the observed spectra. This may indicate the chemical abundances in Abell 14,derived by B03 and H10 using ionization correction factors (ICFs), are uncertain. Gonçalves et al. (2014) pointed out that an additional correction to the ICFs may be necessary when dealing with non-spherical PNe, such as Abell 14. Our results are summarized in Table 2.

Given the observational constraints and the substantial difference between the observed fluxes from B03 and H10, MOD3 reproduces H10's observed spectrum with an acceptable degree of matching. The mismatch of some emission lines shown may be directly associated with the presence of shocks in this nebula, which are not taken into account in our pure photo-ionization model. The typical error of the emission lines is of the order of 15%. The contours from the projected model image (MOD3) are shown overlaid on the observed [N II] λ6584 image in Fig. 8, where the model and observational images appear to be in good agreement. Our best-fit model was obtained for a distance of 4 kpc, whilst the central star has the following atmospheric parameters: $T_{\rm eff} = 120$ kK, log(g) = 7, and $L/L_{\odot} = 15$ with an uncertainty of 10-15%. This suggests that the central source of Abell 14 is a highly evolved star near the white dwarf (WD) cooling track with an evolutionary age around 10^5 yr, according to the evolutionary track from Vassiliadis and Wood (1994) and Blöcker (1995). The former age is much larger than the kinematical age of the nebula of 19,400 yr for a distance of 4 kpc (the best fitting value based on our photo-ionization models). This discrepancy is commonly found in HE–PNe with a WD nucleus such as ESO 166–PN 21 (Peña et al. 1997) and PN S 174 (Tweedy and Napiwotzki 1994). One means by which the age discrepancy may be resolved is if the central source is a close binary system. Such a system would evolve more quickly than a single ionizing central source (Iben and Tutukov 1996). In the case of Abell 14, the observational data are likely consistent with a binary system scenario, but it has not yet been confirmed.

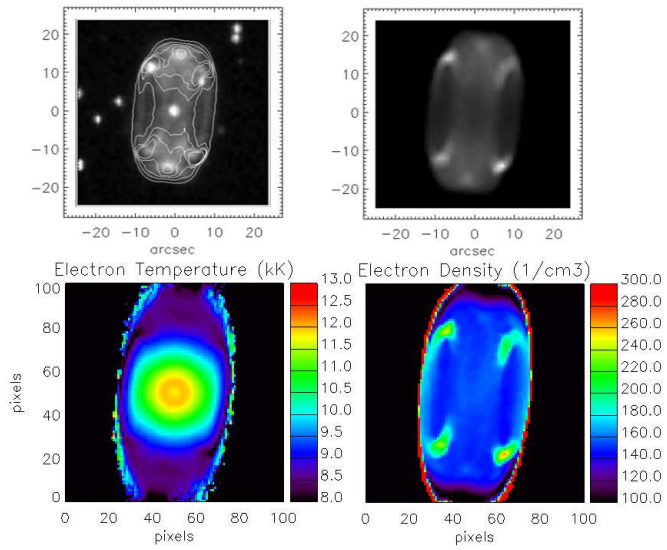

Figure 8. Upper panels: Projected nitrogen λ6584 image obtained from the best–fit model (left) and an observed narrow–band image (right). The white contours are from the model [N II] projected image. Lower panels: Modelled temperature and electron density maps. North is up and east is to the left.

The same model also predicts T_e[N II]=9,300 K, whereas the observed values from B03 and H10 are 12,000 K and 10,500 K, respectively. None of our models were able to reproduce these high T_e, and probably an additional heating mechanism like shocks may have been taken place. The same scenario has also been proposed by B03. The 2D map of the modelled T_e is presented in Fig. 8 (lower left-hand panel), where it shows the stratification of T_e in the nebula. The inner parts are actually hotter than the outer parts by 3000-4000 K. The error of the modelled T_e is between 10-20%, whereas the discrepancy between the model and the observations is between 15-30%. This further supports the scenario of an additional heating mechanism. Besides the T_e discrepancy, the hypothesis of a shock mechanism in this nebula is also evident by the detection of the two neutral lines [N I] λ5200 and [O I] λ6300 emission lines (see Table 2). Our photo-ionization models could not reproduce the intensities of these lines. Nevertheless, bright [N I] λ5200 and [O I] λ6300 lines have also been detected in the HE–PN G342.0–01.7 (Ali et al. 2015). These authors argue that a reverse shock into the nebula, due to the interaction of the nebula with the interstellar medium (ISM), results in the enhancement of the neutral lines. This could also be the case for Abell 14.

We also attempt to reproduce a model assuming a hydrogen-deficient PG 1159 stellar atmospheric model with abundance ratios of He:C:N:O = 33:50:2:15 by mass (MOD4). This model does not provide a good match with the observed spectra, whilst it predicts a very low T_e=6,600 K. We therefore consider that a hydrogen-deficient PG 1159-type star is likely not to be the case for the central source of Abell 14.

Also of importance is the significant discrepancy in the chemical abundances between the studies by B03 and H10. Our best–fit model predicts an N abundance value between both studies, an O abundance close to H10's value, and an S abundance close to that of B03 (see Table 2). The chemical abundances of Abell 14 remain poorly constrained, meriting further study. Despite the significant difference between the chemical abundances, each study agrees that there is a significant N enrichment in the nebula. The N/O ratio is found to be substantially high with values of 3 (B03), 4.13 (H10), 2.85 (MOD3), and 2.66 (MOD4). These values, in conjunction with the high He abundance [0.16 (B03) and 0.196 (H10)], clearly indicate that the progenitor star has experienced the TDU phase. Given that the O abundance is between 2 (B03) and 3 (H10) times lower than the solar value (Asplund et al. 2009), large amounts of O and C must have been converted to N via the CN– and ON–burning cycle (HBB), indicating an intermediate–mass progenitor of $M \geqslant 3\ M_{\odot}$ (Marigo 2007). According to the single star evolutionary tracks of Vassiliadis and Wood (1994), only a star with an initial mass of $\sim 5\ M_{\odot}$, and a sub–solar metallicity (Z = 0.08), would be hot ($T_{\rm eff}$ = 120 kK) and faint enough (L = 15 $L_{\odot}$) to match our findings after ∼85,000 yr. A higher stellar luminosity would result in a younger central star that would be consistent with the kinematical age of the nebula.

5 DISCUSSION

This work presents the first detailed study of the peculiar PN Abell 14 using new high-dispersion echelle spectra and high-resolution images, as well as the astronomical codes SHAPE and MOCASSIN. The former code was used to create the 3D morphology and key features seen in the 2D images and PV diagrams, whereas the latter was used to reproduce its 3D ionization structure, fed by the density distribution obtained with the former.

5.1 Morpho–kinematic structure

Abell 14 has a hollow bipolar shape with the lobes protruding out in the east–west directions. The [N II] emission originates mainly from the walls of the bipolar lobes, whereas the [O III] emission originates from the central region. Two ring–like structures at the eastern and western parts of the nebula are apparent in the Hα and [N II] lines, but are absent in the [O III] line.

The main bipolar shell expands with a velocity that increases with distance from the geometric centre. Adopting an expansion velocity of 21 km s^{-1} for the equatorial region, the kinematical age of the nebula is calculated to be $tD^{-1} = 4,850 \pm 870$ yr kpc^{-1}. A second event likely formed the two ring–like structures that are interacting with the main bipolar component. The kinematical age of the rings is $tD^{-1} = 3,400 \pm 620$ yr kpc^{-1}. Taking into account the lowest (3.32 kpc) and highest (7.25 kpc) available distance measurements of Abell 14 (see §2), we estimate the kinematical ages for the nebula and the rings to range from 16,000 to 35,000 and 11,300 to 24,700 yr, respectively. Adopting the distance of 4 kpc derived from our photoionisation modelling, the kinematical age is 19,400±3,500 yr. We consider this age more reliable.

The morphology of Abell 14 strongly resembles those of other ring-like PNe such as WeBo 1 (Tyndall et al. 2013) and SuWt 2 (Exter et al. 2010, Jones et al. 2010), observed from

Table 3. Chemical abundances† and dereddened emission lines of HE–PNe

PN Name	He	N	O	N/O	[N II]/Hα	[S II]/Hα	[N I]λ5200[a]	[O I]λ6300[a]	Reference
RCW 24	>10.96	8.47	8.03:	2.75	6.1	0.51	–	52	Frew et al. 2006
RCW 69	11.46:	8.70	8.37	2.14	6.9	0.65	29	32	Frew et al. 2006
ESO166–PN21[b]	11.14	>7.75[b]	8.60	0.61[d]	1.7	0.27	–	–	Peña et al. 1997
G342.0–01.7	11.20	8.55	8.54	1.01	4.15	0.60	24	55	Ali et al. 2015
HaTr 10	–	8.70	8.00	5.01	6.33	0.53	–	–	Tajitsu et al. 1999
SBW 1	–	>7.20[c]	–	–	0.6	0.13	–	–	Smith et al. 2007
SBW 2	–	>8.13[c]	–	–	7.42	0.58	–	86.6	Smith et al. 2007
SuWt 2	–	>8.40[c]	–	–	8.21	0.81	–	59.2	Smith et al. 2007
SuWt 2††	10.92	8.60	8.6	0.82	4.70	0.41	–	119[e]	Danehkar et al. 2013
WeBo 1	–	>8.11[c]	–	–	2.63	0.09	–	41.6	Smith et al. 2007
G321.6+02.2	11.17	9.22	8.75	2.95	12.27	0.79	16.24[f]	30.57[f]	Corradi et al. 1997
Abell 14	11.20	8.59	8.11	3.02	6.69	0.35	29	–	B03
Abell 14	11.29	9.02	8.41	4.07	7.52	0.40	–	30	H10
Abell 14††	11.20	8.78	8.32	2.88	6.67	0.43	–	–	this work (MOD3)
Abell 14††	11.20	8.90	8.48	2.63	6.34	0.26	–	–	this work (MOD4)
Type–I	11.14	8.77	8.76	1.03	Fig. 9	Fig. 9	–	–	Henry et al. 2004
Type–II	11.05	8.20	8.70	0.31	Fig. 9	Fig. 9	–	–	Henry et al. 2004
The Sun	10.93	7.83	8.69	0.14	–	–	–	–	Asplund et al. 2009

† Chemical abundances are given in the notation of 12+log[n(X)/n(H)], †† These values have been derived from photo–ionization models.
[a] Relative to Hβ = 100, [b] Average value from 7 slit positions, [c] This value is a lower limit and corresponds only to N^+.
[d] This ratio was calculated based on the assumption of $N/O = N^+/O^+$, [e] The night sky emission line at 6300Å may have not been properly subtracted. [f] They have been dereddened using R = 3.1

different orientations. A comprehensive study involving several circumstellar rings has also been performed by Smith et al. (2007). These authors conclude that ring–like structures are divided into two groups: i) those that are formed around massive supergiants, like SN 1987A (Meaburn et al. 1995, Panagia et al. 1996) and ii) those around intermediate–mass stars in close binaries, like SBW 1 (Smith et al. 2007). The bipolar structure of Abell 14 is more consistent with the second scenario, although the binary system has not been yet confirmed as in the cases of WeBo 1 and SuWt 2.

In particular, WeBo 1 is a member of a small group of PNe (Abell 35, Abell 70, LoTr 1, and LoTr 5) whose central stars share several common properties (Bond et al. 1993, 2003). Their central stars are binary systems with a rapidly rotating giant or sub–giant and a hot, optically faint companion. Siegel et al. (2012) photometrically confirmed the binary nature of WeBo 1. Lutz & Kaler (1987) and Weidmann & Gamen (2011) proposed the presence of a binary system in Abell 14 in order to explain the observational data. Morphologically, WeBo 1 clearly shows a ring–like structure in the Hα+[N II] emission lines, whereas the [O III] emission is more diffuse in the inner region, like what we observe in Abell 14 (see Fig. 11 from Tyndall et al. 2013).

As for SuWt 2, it also exhibits a bright ring–like structure with much fainter bipolar lobes, seen almost edge–on (Exter et al. 2010, Jones et al. 2010). Its morphology is similar to that found in WeBo 1 and Abell 14, whilst its central star has been classified as a B9 or early A–type star (Exter et al. 2010). Such a cool star emits insufficient amounts of ionizing radiation, which suggests the presence of a hotter binary companion, as recently confirmed by Exter et al. (2010). Given the noticeable similarities among Abell 14, WeBo 1, and SuWt 2, they may be similar objects.

5.2 Ionization structure and the central star

The 3D density distribution grid, derived using SHAPE, was used as an input to the MOCASSIN code in order to perform a more comprehensive study of its ionization structure. Two available spectra from the literature were used to constrain the models. It is worth pointing out that this technique of deriving independent density grids has also been applied to NGC 1501 by Ercolano et al. (2004) using a density grid derived from long-slit echellograms as an input to MOCASSIN and also to NGC 40 by Monteiro and Falceta-Gonçalves (2011), using a density distribution derived from 2.5D hydrodynamic simulations.

Two models were run with the chemical abundances as free parameters and assuming a stellar model atmosphere (MOD3) and a hydrogen-deficient, PG 1159 stellar atmosphere model (MOD4) for the central source. Both models adequately reproduced the majority of the emission lines (Table 2) for a distance of 4 kpc. The stellar parameters (L = 15 $L_\odot$, log(g) = 7, and $T_{\rm eff}$ = 120 kK) indicate a highly evolved central star near to the cooling track of WDs. In accordance with the theoretical hydrogen-burning evolutionary track of Vassiliadis and Wood (1994), the central star has an evolutionary age of ∼85,000 yr (for M = 5 $M_\odot$ and Z = 0.08), which is several times higher than the kinematical age of the nebula (∼19,400 yr). Nevertheless, this discrepancy is a common problem in evolved PNe with highly evolved central stars (e.g. Peña et al. 1997). A possible solution is the interaction between two binary components that would

Table 4. Stellar and physical parameters of HE–PNe.

PN Name	$T_{\rm eff}$ (kK)	L ($L_{\odot}$)	log(g)	$N_{\rm e}$ (cm^{-3})	D (kpc)	Kinematical age (yr)	Reference
RCW 24	∼120	70	–	<100	1	> 26,000[a]	Frew et al. 2006
RCW 69	∼130	190	–	250	1.3	> 17,000[a]	Frew et al. 2006
ESO 166–PN21	69.2	22	7.14	∼100	1.19	16,100	Peña et al. 1997
G342.0–01.7	105	118	7	<20	2.06	⩾ 20,000	Ali et al. 2015
HaTr 10	100	47	–	580	1.5	> 17,000[a]	Tajitsu et al. 1999
SBW 1	–	–	–	513	7	9,600	Smith et al. 2007
SBW 2	–	–	–	280	2.3	> 26,000	Smith et al. 2007
SuWt 2[†b]	160	600	7.3	<100	2.3	23,400–26,300	Danehkar et al. 2013
WeBo 1	–	–	–	312	1.6	11,700-12,000	Tyndall et al. 2013, Bond et al. 2003
G321.6+02.2	>130	–	–	250	2	> 12,000	Corradi et al. 1997
Abell 14[†]	120	15	7	100-180	4	19,400	this work

[†] The stellar parameters have been derived from photo–ionization models.
[a] These kinematical ages have been calculated by us, assuming a nominal expansion velocity of 40 km s^{-1}.
[b] A possible born–again PN.

accelerate the evolution of the system (Iben and Tutukov 1986). Given that the star at the centre of the nebula has been classified as a B–type massive blue giant (B5 III–V, Lutz & Kaler 1987; B8-9, Weidmann & Gamen 2011), the presence of a binary system in Abell 14 is very possible. The helium–burning evolutionary track (very late thermal pulse) gives for the aforementioned stellar parameters an extremely high evolutionary age, that is between 200,000–300,000 yr. This age is 3-4 times larger than the evolutionary age based on hydrogen-burning tracks and at least 10 times larger than the kinematical age of the nebular gas. Notice that SuWt 2, a likely born-again nebula (Danehkar et al. 2013), is one of the oldest member in our sample of HE-PNe, based on its kinematical age, but at the same time it is the most luminous. This indicates that the central star of SuWt 2 is in an earlier evolutionary stage than all other members (see Table 4). According to this analysis, Abell 14's stellar parameters (L = 15 $L_{\odot}$, $T_{\rm eff}$ = 120 kK) and its kinematical age (∼19,400 yr) cannot be explained by the born-again scenario, which should result in a much older nebula, for the given stellar parameters.

Our two best–fit models and the observed spectra agree that there is significant He and N abundance enrichment in Abell 14. Based on the Kingsburgh and Barlow (1994) classification scheme, Abell 14 is an extreme Type–I highly evolved nebula and probably one with the largest He abundance and N/O ratio. These values are consistent with a 5 $M_{\odot}$ progenitor derived from the evolutionary tracks.

5.3 Comparison of Abell 14 and other highly-evolved PNe

Until now, only a small number of studies have been performed on highly evolved Type–I PNe (see Tables 3 & 4). All PNe in this group show substantially high N/O ratios and He abundances whilst their central stars have very low L and high $T_{\rm eff}$, and they are possible descendants of intermediate-mass stars in close binaries. Only the central star of SuWt 2 has a high luminosity of 600 $L_{\odot}$ and a large kinematical age (Danehkar et al. 2013), due to a likely very late thermal pulse (born–again scenario). Moreover, while most HE–PNe show N/O ratio larger than 1 (N rich), SuWt 2 has an N/O = 0.8 which makes it somewhat different.

Most of the HE–PNe in our group (Tables 3 and 4) lie in the low-left corner of the PNe regime on the Hα/[N II] vs. Hα/[S II] diagnostic diagram (Sabbadin et al. 1977; Gonçalves et al. 2003) of Galactic PNe (Fig. 9). Akras & Gonçalves (2016) have recently demonstrated that in this regime also lie shock–excited regions, e.g. low–ionization structures such as knots and jets. Since these PNe do not exhibit high velocities, the scenario of shocks in such large and HE–PNe seems unlikely. Interestingly, some HE–PNe exhibit uncommonly bright [N I] λ5200 and [O I] λ6300 emission lines, which are strong indicators of shock activity. Recently, Ali et al. (2015) showed that a reverse shock of only 25 km s^{-1} in the PN G342.0–01.7, due to its motion through the ISM, can successfully explain the strong neutral emission lines. The low photo–ionization rate of their central stars, (very low L) and large nebular size, would make the contribution of shocks easily perceptible even at small velocities (Akras & Gonçalves 2016), or produce emission line spectra that resemble those of shock-excited regions (Raga et al. 2008).

Three out of 11 HE–PNe are seen to exist outside the normal region in Fig. 9, namely SBW 1, ESO 166–PN 21, and WeBo 1. SBW 1 and WeBo 1 are the youngest members in this group, and their central stars are such luminous that their high photo-ionization rate overcomes the shock excitation. Unfortunately, the stellar parameters of these HE–PNe are still unknown. Regarding ESO 166–PN 21, the [N II]/Hα and [S II]/Hα line ratios correspond to an average value from 7 slit positions (for more details see in Peña et al. 1997). Studying the spectrum of each slit position separately, we deduce that the most distant regions (A1 and A5 in Peña et al. 1997) exhibit stronger [N II] and [S II] lines. Two out of 7 regions in ESO 166–PN 21 lie in the regime of HE–PNe. This is in agreement with our previous analysis that the lower the photo-ionization rate, the stronger the low–emission lines (Raga et al. 2008, Akras & Gonçalves 2016).

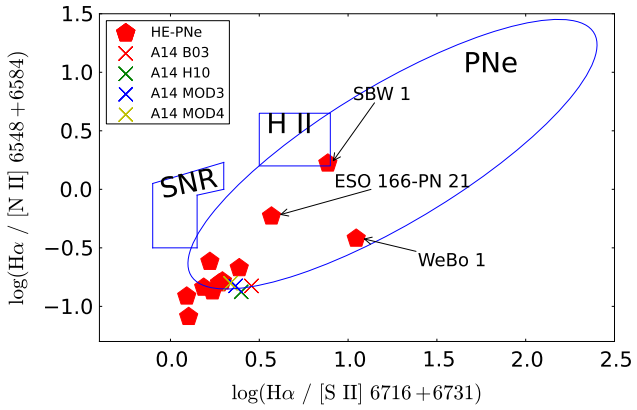

Figure 9. A diagnostic diagram of Galactic PNe by Sabbadin et al. (1977) with the density ellipses introduced by Riesgo & López (2006) and for the HE–PNe in Tables 3 and 4.

6 CONCLUSIONS

The first detailed study of the 3D morphology and ionization structure of Abell 14 has been discussed in this paper. The kinematical and physical parameters of this nebula, as well as the stellar parameters of its central source have been derived using new high-dispersion spectroscopic data and high-resolution images, as well as the 3D codes SHAPE and MOCASSIN. The resultant modelled 3D density distribution obtained from SHAPE has been used as an input to the MOCASSIN code. To successfully create a photo-ionization model using the proposed technique (SHAPE + MOCASSIN), at least two emission lines (e.g. [N II] and [O III]) are required to constrain the morphology of the inner and outer parts, while obtaining a 3D density distribution that best describes the entire nebula.

Abell 14 was found to be a highly evolved (19,400 yr), Type–I PN (11.20 < He < 11.29, and 2.63 < N/O < 4.03) formed by an intermediate-mass progenitor of 5 $M_{\odot}$, which it has likely experienced the TDU and HBB, resulting in a substantial enrichment of He and N. The abundance of O is found to be sub–solar, indicating that large amounts have been converted to N. The synthetic PV diagrams and 2D image from the SHAPE code at different orientations resemble the structure of WeBo 1 and SuWt 2, thus suggesting that these are objects with similar morphologies observed from different angles. The binary companion of the central star in WeBo 1 and SuWt 2 has already been confirmed, but not for the central source in Abell 14. The bright star at the centre of Abell 14 has been classified as a massive blue-giant; but such star is not hot enough to ionize the surrounding gas, making a second, hotter companion probable. Our best–fit ionization models adequately reproduced the observed spectra for a central source with $T_{\rm eff}$ = 120 kK and L = 15 $L_{\odot}$. These stellar parameters can not be explained by the born-again scenario within an evolutionary timescale of ∼85,000 yr (hydrogen burning timescale). The central star of Abell 14 is in a more evolved evolutionary phase than that of SuWt 2, a likely born-again nebula. while it is surrounded by a younger nebula (lower kinematical age). This implies that the central star of Abell 14 has not experienced any very late thermal pulse event.

Returning to the shaping mechanisms of bipolar planetary nebulae, this study indicates that a highly evolved, low luminosity and intermediate mass progenitor, within a binary system is responsible for the distinctive double-ringed structure and peculiar spectrum observed in Abell 14.

Abell 14 also shows unexpectedly strong [O I] λ6300 and [N I] λ5200 emission lines that are not reproducible by our photo–ionization models. This indicates that shock interactions may play an important role. The very low luminosity of its central star, in conjunction with the nebula's large size, imply a very low photo–ionization rate that makes the contribution of shocks easily perceptible. Regarding its [N II]/Hα and [S II]/Hα line ratios, Abell 14 seems to have some similarities with supernova remnants, but it is more closely related to other HE-PNe.

Of all HE–PNe discussed here, 8 out of 11 exhibit strong neutral [O I] λ6300 line, likely associated with shocks, 6 out of 7 have central stars with L < 200 $L_{\odot}$, and are therefore at a very evolved stage near the WD cooling track with very low photo-ionization rates. We argue that any shock interaction due to stellar winds, or interaction between the nebula and the surrounding ISM (e.g. G342.0-01.7) may be the main reason for the enhancement of the low-ionization lines.

ACKNOWLEDGMENTS

We also thank the anonymous referee for her/his thorough review and helpful comments. The authors would like to thank the staff at SPM and Helmos Observatories for their excellent support during these observations. The Aristarchos telescope operated on Helmos Observatory by the Institute of Astronomy, Astrophysics, Space Applications and Remote Sensing of the National Observatory of Athens. SA is supported by CAPES post–doctoral fellowship 'Young Talents Attraction' – Science Without Borders, A035/2013. NC gratefully acknowledges the support of the College of Science, NUI Galway (under their PhD fellowship scheme). CHIANTI is a collaborative project involving George Mason University, the University of Michigan (USA) and the University of Cambridge (UK).

REFERENCES

Abell G. O., 1966, ApJ, 144, 259
Akras S., Steffen W., 2012, MNRAS, 423, 925.
Akras S., López J. A., 2012, MNRAS, 425, 2197
Akras S., Gonçalves D. R., 2016, MNRAS, 455, 930
Ali A., Amer M. A., Dopita M. A., Vogt F. P. A., Basurah H. M., 2015, A&A, 583, 83
Asplund M., Grevesse N., Sauval A.-J., Scott P., 2009, ARA&A, 47, 481
Balick B., Frank A., 2002, A&A Annual Review, 40, 439
Blöcker T., 1995, A&A, 299, 755
Bohigas J., 2003, Rev. Mex. Astron. Astrofis., 39, 149.
Bond H. E., Ciardullo R., Meakes M. G., 1993, in IAU Symp. 155, Planetary Nebulae, ed. R. Weinberger & A. Acker (Dordrecht: Kluwer), 397
Bond H. E., Pollacco D. L., Webbink R. F., 2003, AJ, 125, 260–264.

Boumis P., Akras S., Xilouris E. M., et al., 2006, MNRAS, 367, 1551
Boumis P., Paleologou E. V., Mavromatakis F., Papamastorakis J., 2003, MNRAS, 339, 735
Cahn J. H., Kaler J. B., Stanghellini L., 1992, A&AS, 94, 399
Chevalier R. A., Luo D., 1994, ApJ, 421, 225
Clyne, N., Redman, M. P., Lloyd, M., et al. 2014, A&A, 569, A50
Clyne N., Akras S., Steffen W., Redman P. M., D. R. Gonçalves R. D., Harvey E., 2015, A&A, 582, 60
Corradi R. L. M., Villaver E., Mampaso A., Perinotto M., 1997, A&A, 324, 276
Danehkar A., Parker Q. A., Ercolano B., 2013, MNRAS, 434, 1513
de Marco O., 2009, PASP, 121, 316
Ercolano B., Barlow M. J., Storey P. J., Liu X.–W., 2003, MNRAS, 340, 1136
Ercolano B., Wesson R., Zhang Y., Barlow M. J., De Marco O., Rauch T., Liu X.-W., 2004, MNRAS, 354, 558
Ercolano B., Barlow M. J., Storey P. J., 2005, MNRAS, 362, 1038
Ercolano B., Young P. R., Drake J. J., Raymond J. C., 2008, ApJS, 175, 534
Exter K., Bond H. E., Stassun K. G., Smalley B.; Maxted P. F. L., Pollacco D. L., 2010, AJ, 140, 1414.
Frew, D. J., Parker, Q.A., Russeil, D. 2006, MNRAS, 372, 1081
Frew D. J., Bojičić I. S., Parker Q. A., 2013, MNRAS, 431, 2
Frank A., Blackman E. G., 2004, ApJ, 614, 737
García–Segura G., López J. A., 2000, ApJ, 544, 336
García–Segura G., Villaver E., Langer N., Yoon S.-C., Manchado A., 2014, AJ, 783, 74
Giammanco C., Sale S. E., Corradi R. L. M., Barlow M. J., Viironen K., et al., 2011, A&A, 525A, 58
Gonçalves D. R., Corradi R. L. M., Mampaso A., Perinotto M., 2003, ApJ, 597, 975
Gonçalves D. R., Wesson R., Morisset C., Barlow M., Ercolano B., 2014, Asymmetrical Planetary Nebulae VI conference, Proceedings of the conference held 4-8 November, 2013, Edited by C. Morisset, G. Delgado-Inglada and S. Torres-Peimbert. Online at http://www.astroscu.unam.mx.
Henry R. B. C., Kwitter K. B., Balick B., 2004, AJ, 127, 2284
Henry R. B. C., Kwitter K. B., Jaskot A. E., Balick B., Morrison M. A., Milingo J. B., 2010, ApJ, 724, 748
Iben I., Tutukov A., 1986, ApJ 311, 742
Iben I. Jr., Livio M., 1993, PASP, 105, 1373
Jones D., Lloyd M., Mitchell D. L., Pollacco D. L., OBrien T. J., Vaytet N. M. H., 2010, MNRAS, 401, 405
Jones D., Mitchell D. L., Lloyd M., 2012, MNRAS, 420, 2271
Jones D., Boffin H. M. J., Rodríguez–Gil P., Wesson R., Corradi R. L. M., Miszalski B., Mohamed S., 2015, A&A, 580, 19
Kingsburgh R. L., Barlow M. J., 1994, MNRAS, 271, 257
Kwitter K. B., Méndez R. H., Peña, M., Stanghellini L., Corradi R. L. M., et al., 2014, RMxAA, 50, 203
Kwok S., Purton C. R., Fitzgerald P. M., 1978, ApJ, 219, 125
Landi E., Del Zanna G., Young P. R., Dere K. P., Mason H. E., 2012, ApJ, 744, 99
Lutz J. H., Kaler J. B., 1987, BAAS, 19, 1090
Manchado A., Garcá–Hernández D. A., Villaver E., Guironnet de Massas J., 2011, ASPC, 445, 161.
Meaburn J., Bryce M., Holloway A. J., 1995, A&A, 299, 1
Meaburn J., López J. A., Gutiérrez L., Quiróz F.; Murillo J. M., Valdéz, J., Pedrayez M., 2003, Rev. Mex. Astron. Astrofis., 39, 185.
Miszalski B., Corradi R. L. M., Boffin H. M. J., Jones D., Sabin L., Santander–García M., Rodríguez-Gil P., Rubio–Díez M. M., 2011a, MNRAS, 413, 1264
Miszalski B., Jones D., Rodríguez-Gil P., Boffin H. M. J., Corradi R. L. M., Santander-García M., 2011b, A&A, 531, 158
Monteiro H., Falceta-Gonçalves D., 2011, ApJ, 738, 174
Nordhaus J., Blackman E. G., Frank A., 2007, MNRAS, 376, 599
Panagia N, Scuderi S., Gilmozzi R., Challis P. M., Garnavich P. M., Kirshner R. P., 1996 AJ, 459, 17–21.
Parker Q. A., et al., 2006, MNRAS, 373, 79
Peña M., Ruiz M.T., Bergeron P., Torres–Peimbert S. and Heatcote S., 1997, A&A, 317, 911
Phillips J. P., 2004, MNRAS, 353, 589
Rauch T. 2003, A&A, 403, 709
Raga A. C., Riera A., Mellema G., Esquivel A., Velázquez P. F., 2008, A&A, 489, 1141
Riesgo H., López J. A., 2006, RMxAA, 42, 47
Sabbadin F., Minello S., Bianchini A. 1977, A&A, 60, 147
Sabin L., Parker Q. A., Corradi R. L. M., et al., 2014, MNRAS, 443, 3388
Sahai R., Morris M. R., Villar G. G., 2011, AJ, 141, 134
Siegel M. H., Hoversten E., Bond H. E., Stark M., Breeveld A. A., 2012, AJ, 144, 65
Smith N., Bally J., Walawender J., 2007, AJ, 134, 846
Soker N., Livio M., 1994, ApJ, 421, 219
Soker N., Rappaport S., 2001, ApJ, 557, 256
Soker N., 2006, PASP, 118, 260
Stanghellini L., Haywood M., 2010, ApJ, 714, 1096
Steffen W., López J. A., 2006, Rev. Mex. Astron. Astrofis., 42, 99
Steffen W., Koning N., Wenger S., Morisset C., Magnor, M. 2011, IEEE Transactions on Visualization and Computer Graphics, 17, 454
Tajitsu A., Tamura S., Yadoumaru Y., Weinberger R., K oppen J., 1999, PASP, 111, 1157
Tyndall A. A., Jones D., Boffin H. M. J., Miszalski B., Faedi F., Lloyd M., López J. A., Martell S., Pollacco D., Santander–Garc´a M., 2013, MNRAS, 436, 2082
Tweedy R. W., Napiwotzki R., 1994, AJ 108, 978
Vassiliadis E., Wood P. R. 1994, ApJS, 92, 125
Vlemmings W., 2012, IAU Symp, 283, 176–179
Weidmann W. A., Gamen R., 2011, A&A, 531A, 172
Zhang C. Y., 1995, ApJS, 98, 659